HHS Public Access

Author manuscript

Ultrasonics. Author manuscript; available in PMC 2023 February 01.

Published in final edited form as:

Ultrasonics. 2022 February ; 119: 106591. doi:10.1016/j.ultras.2021.106591.

Acoustic properties across the human skull

Thomas S. Riis, **Taylor D. Webb**, **Jan Kubanek**

Department of Biomedical Engineering, University of Utah, Salt Lake City, 84112, UT, United States

Abstract

Transcranial ultrasound is emerging as a noninvasive tool for targeted treatments of brain disorders. Transcranial ultrasound has been used for remotely mediated surgeries, transient opening of the blood-brain barrier, local drug delivery, and neuromodulation. However, all applications have been limited by the severe attenuation and phase distortion of ultrasound by the skull. Here, we characterized the dependence of the aberrations on specific anatomical segments of the skull. In particular, we measured ultrasound propagation properties throughout the perimeter of intact human skulls at 500 kHz. We found that the parietal bone provides substantially higher transmission (average pressure transmission 31±7%) and smaller phase distortion (242±44 degrees) than frontal (13±2%, 425±47 degrees) and occipital bone regions (16±4%, 416±35 degrees). In addition, we found that across skull regions, transmission strongly anti-correlated ($R = -0.79$) and phase distortion correlated ($R = 0.85$) with skull thickness. This information guides the design, positioning, and skull correction functionality of next-generation devices for effective, safe, and reproducible transcranial focused ultrasound therapies.

Keywords

transcranial ultrasound; skull; transmission; attenuation; phase; thickness

PACS:

0000; 1111

2000 MSC:

0000; 1111

1. Introduction

Transcranial focused ultrasound offers incisionless and targeted treatment options for disorders of brain function [1–3]. At high intensities, ultrasound has been used to lesion

tom.riis@utah.edu (Thomas S. Riis).

malfunctioning or diseased deep brain targets [4, 5]. At low intensities, ultrasound can be used to deliver large drugs, genes, or stem cells across the blood-brain barrier [6–9]; release drugs in specific brain regions without affecting the blood-brain barrier [10–13]; and to modulate neural activity in a transient [14–17] or sustained [18–25] fashion.

The clinical utility of these applications has been impeded by the severe aberrations of ultrasound by the human skull. In the surgical applications, the highly variable attenuation and phase distortions can leave a substantial proportion of patients untreated [26]. The skull aberrations have limited the predictability of the ultrasound magnitude delivered into target [27] and so have also impeded the translation of low-intensity applications. A tight control of the delivered dose is particularly important for ultrasound-mediated opening of the blood-brain barrier, in which small changes in the ultrasound pressure at target—on the order of 10–20%—can lead to vast differences in the scale of the blood-brain barrier disruption [6, 28]. The skull aberrations have also curbed effective and reproducible applications of ultrasonic neuromodulation [29, 30] and local drug release, which require a well-defined ultrasound dose [11, 31].

To maximize ultrasound penetration through the skull and to maximize the predictability of the delivered dose, ultrasound should be applied through skull segments that cause the least amount of attenuation and phase distortion. In diagnostic applications, small imaging probes can be applied through the temporal window, which has a relatively low ultrasound attenuation [32–36]. However, therapeutic applications often require large apertures or arrays with many elements for focal delivery of considerable amount of energy [4, 18, 19, 29, 37–40]. Any future design that maximizes ultrasound penetration and the predictability of the delivered dose should take into account the dependence of the aberrations on specific anatomical regions of the skull.

This information is currently incomplete. Existing studies have provided insights into inter-subject variability of acoustic properties [32, 41–44], estimates of average attenuation and phase distortions [32, 41–50], as well as approaches on how these aberrations may be compensated for [4, 51–57]. However, acoustic measurements have only been provided for discrete sets of chosen samples or skull flaps [32, 41–45]. Consequently, there is no systematic assessment of acoustic propagation properties within single intact skulls as a function of anatomical location.

To address this, we devised a setup that allowed us to measure ultrasound propagation properties throughout the perimeter of intact human skulls. We complemented these acoustic measurements with caliper measurement of the corresponding skull thickness. The resulting data quantify the transmission and phase distortion through anatomically defined segments of the skull, and show how these variables depend on the skull thickness. This information guides the design and placement of future devices for effective applications of transcranial ultrasound in the clinics.

2. Materials and Methods

2.1. Subjects

Three *ex-vivo* skulls were used in this study (Skull 1: male, 84 years; Skull 2: male, 61 years; Skull 3: female 68 years). The skulls were obtained under a research agreement from Skulls Unlimited (Oklahoma City, OK). An opening was made at the bottom of each skull to enable skull rotation around a receiving transducer positioned inside the skull.

Each skull was degassed overnight in a deionized water. Degassing is a standard procedure that removes trapped air in the porous cancellous bone which is filled with blood and fat in-vivo [41, 50, 58–60]. Following the degassing, the skull was transferred, within the degassed water, into an experimental tank filled with continuously degassed water (AIMS III system with AQUAS-10 Water Conditioner, Onda). The water conditioner (AQUAS-10) treats water for ultrasound measurements in compliance with IEC 62781. The conditioner degasses water to remove undesired bubbles, removes suspended particles and biological contaminants, and deionizes water. The dissolved oxygen is between 2.0–2.5 PPM during continuous operation, according to measurements provided by the manufacturer (Onda). In comparison, tap water contains about 10.5 PPM of dissolved oxygen.

The skull was held in place by a pair of thin neodymium rare earth magnets (550lbs lift, 2.5-inch diameter, Neosmuk), one positioned below the skull and one above, at the center of the sagittal suture. The magnets allowed us to firmly hold and rotate each skull without having to perturb its surface.

2.2. Coordinates

Prior to degassing, the through-transmit plane was established using 4 markers that were chosen such as to avoid frontal and sphenoidal sinuses and to maintain perpendicular ultrasound propagation. Specifically, a frontal marker was positioned 49 mm above the center of the nasion. Two parietal markers, one on the left and one on the right, were made 17 mm above the squamous suture and at the widest point of the skull. The final, occipital marker was made approximately 17 mm above the center of the inion. An angular positioner assembly (AP02-S, Onda) was aligned with the 4 markers in the following way: the frontal marker corresponded to 0 degrees, the right parietal marker to 90 degrees, the occipital marker to 180 degrees, and the left parietal marker to 270 degrees (Fig. 1b).

2.3. Skull thickness measurements

To measure skull thickness, the 4 markers were connected with a line. A precision caliper gage (Fowler 54-554-630, 0.1 mm accuracy) was used to measure the thickness of the skull in 3 mm steps. Each measurement was repeated 3 times after fully retracting and re-positioning the caliper in each measurement to gauge non uniformity of the skull section thickness; the resulting values were averaged together. Only rarely was there a difference of more than 0.1 mm between the 3 measurements. The standard deviation of all measurements was 0.07 mm. The thickness measurements may have incurred additional error due to the imperfect alignment between the outer and inner surface and the natural curvature of the skull. Such errors were assumed to be minimal as in previous studies [49, 61].

2.4. Through-transmit setup

Two transducers operating at 500 kHz center frequency (V301-SU, Olympus, unfocused, 28.5 mm face diameter) were mounted to a breadboard such that they faced each other. One transducer served as a transmitter and one as a receiver. The distance between the transducers' faces was 100 mm. The breadboard with the mounted transducers was positioned at the bottom of the water tank. The center of each face of the transducer was 145 mm above the breadboard. Each skull was electronically translated and rotated such that 1) the line connecting the centers of the two transducers intersected with the 4 markers 2) all segments of the skull were in the far field of the transmitting transducer (at a distance greater than 68.6 mm). The beam width of our unfocused transducer at the skull was calculated as: FWHM = $0.704\ \lambda\ z/a = 10\ mm$, where λ is wavelength, z is axial distance from the transducer face, and a is radius of the transducer. Across this length, the deviation in skull thickness is considered negligible [61]. The acoustic pathway connecting the centers of the two transducers was determined using a custom 3D printed plastic pointer positioned into the holder of the transmitting transducer. We used 3D CT images of the skull to measure the incident angles for each measured skull segment. The incident angle was taken as the angle between the acoustic path and the normal vector of the skull surface at that point. The mean+−SD incidence angle was 7.3+−4.9 degrees. Incidence angles within this range have only minimal impact on the measurements and do not affect our conclusions [41].

2.5. Ultrasound system and pulses

The through-transmit protocol was implemented on the Vantage256 system (Verasonics), using a custom matlab script. We used chirp pulses of 3 distinct forms. Chirps are frequency-modulated waveforms that have a narrow autocorrelation function. A narrow autocorrelation function maximizes the accuracy of the detection of time delays in through-transmit procedures [62, 63]. Chirp3 consisted of three consecutive cycles of [0.75, 1, 1.25] times the center frequency of 500 kHz. Chirp4 consisted of four consecutive cycles with [0.75, 1, 1.25, 1.5] times the center frequency. Chirp5 consisted of five consecutive cycles with [0.5, 0.75, 1, 1.25, 1.5] times the center frequency. Our transducers were broadband (Videoscan series, Olympus) and so capable of emitting the frequency spectrum. Each pulse was transmitted and detected 32 times; the responses were averaged together.

2.6. Through-transmit procedure

The through-transmit procedure quantifies the changes in amplitudes and received times following an introduction of an object (e.g., skull) into the transmit-receive path. Data were first collected in water. This provided an average no-skull receive waveform. Consequently, the skull was lowered into a location described above, and gradually rotated in 1 degree increments, with the through-transmit data taken at each. This provided through-skull receive waveforms. The maximum of each through-skull receive waveform divided by the maximum of the no-skull receive waveform provided the relative pressure transmission, separately for each angle (Fig. 3, Fig. 5). To determine the time shift, a cross-correlation was computed between the no-skull and through-skull receive waveforms, separately for each angle. The peak of the cross-correlation defined the time shift. This time corresponds to the

speedup values shown in Fig. 6 and Fig. 7. The three pulses produced equivalent values of time shift in most cases. These values were averaged together.

2.7. Through-transmit relationships

The ultrasound speedup through a skull segment τ is mathematically proportional to the thickness of the segment h through:

$$\tau = h\left(\frac{1}{c_w} - \frac{1}{c_s}\right),$$

where c_w = 1481 m/s is the speed of sound through water, and c_s is the average speed of sound through the skull segment. The phase distortion or shift caused by the speedup is equal to $\omega\tau$, where ω is the angular frequency.

The measured pressure transmission (T) depends on ultrasound reflection from the individual layers of the skull and on a set of attenuation factors (α) that include ultrasound absorption and scattering. Under an assumption that these factors can be considered separate and independent, we can write:

$$T = R\exp(-\alpha h),$$

where R is the loss due to reflection and h is the skull segment thickness. Taking a logarithm of this equation yields:

$$\ln = T = \ln(R) - \alpha h\,.$$

The set of thickness-dependent attenuation factors α can be inferred as a slope of the relationship between ln(T) and h (Fig. 5).

3. Results

We assessed the acoustic properties across intact *ex-vivo* human skulls using an apparatus that allowed controlled rotation about a central axis (Fig. 1). The acoustic properties were characterized using standard through-transmit measurements (Materials and Methods), with the transmitting/receiving transducer positioned outside/inside of the skull. The position of the two transducers was fixed; only the skull was rotated. The through-transmit values obtained through the skull were compared to free-field values in which no skull was present, as in previous studies [41, 55].

We performed the through-transmit measurements in three degassed and hydrated *ex-vivo* skulls. The CT images of the skulls within the through-transmit plane are shown in Fig. 2.

The relative pressure transmission across the individual anatomical locations is shown in (Fig. 3). The figure reveals that the highest transmission was observed in segments centered over the parietal bone. The average transmission in the parietal regions was 2.4 higher than in the temporal regions and 2.0 higher than in the occipital regions (Table 1). The

transmission was maximal within the parietal bone and delivered an average 41.6% of the ultrasound pressure across the three skulls. As apparent from the figure, the transmission varied substantially across the 3 subjects—the 3 skulls showed an average 22.2%, 16.8%, and 29.5% transmission, respectively. Effects of the skull position and subject were both significant. In particular, a two-way ANOVA revealed a significant modulation of the pressure transmission by the skull position ($F(360, 720) = 7.48$, $p = 4.7 \times 10^{-115}$) and by subject ($F(2, 720) = 353.90$, $p = 9.1 \times 10^{-108}$).

We measured the thickness of the skulls across the through-transmit plane using a caliper (see Materials and Methods). The skull thickness as a function of position is shown in Fig. 4. The figure reveals a substantial variability in skull thickness within and across individuals. The thickness ranged from 3.1 mm to 14.0 mm, with an average of 6.5 mm and a standard deviation of 1.7 mm. The parietal bone was on average thinner than the frontal and occipital bones (Table 1). The thickness varied across the 3 subjects, with average values of 5.6 mm, 6.4 mm, and 7.5 mm, respectively. A two-way ANOVA revealed a significant modulation of thickness by the skull position ($F(66, 332) = 3.75$, $p = 7.2 \times 10^{-25}$) and by subject ($F(2, 332) = 64.96$, $p = 1.6 \times 10^{-24}$).

The profiles of pressure transmission (Fig. 3) and skull thickness (Fig. 4) suggest an inverse relationship between these quantities: the thinner the skull, the more effective the transmission. Indeed, we found that skull thickness is a strong predictor of the transmission efficacy (Fig. 5). In the three skulls, skull thickness explained 45%, 65%, and 81% of the variance in the pressure transmission, respectively. An ANCOVA model, with a continuous factor of skull thickness and a discrete factor of subject, found a significant effect of thickness ($F(1, 495) = 974.45$, $p = 4.9 \times 10^{-119}$) as well as an effect of subject ($F(2, 495) = 161.15$, $p = 1.3 \times 10^{-54}$) and thickness×subject interaction ($F(2, 495) = 90.31$, $p = 3.7 \times 10^{-34}$). Thus, there is a significant difference in the pressure transmission across the subjects, and the dependence of transmission on skull thickness is subject-specific. We further investigated the thickness dependence of the natural logarithm of the pressure transmission. The logarithmic formulation may enable the quantification of skull thickness-dependent attenuation factors α from the slope of the linear relationships showed in the bottom part of Fig. 5 (see Materials and Methods). The slopes for the 3 skulls were −0.176, −0.489, and −0.208, respectively. According to the simple—though likely simplistic—model (Materials and Methods), this slope translates into thickness-dependent attenuation factors of $\alpha = 176$ Np/m, $\alpha = 489$ Np/m, and $\alpha = 208$ Np/m, respectively.

It is known that the skull speeds up the propagation of ultrasound compared to water. This relative speedup leads to distortions or shifts of the ultrasound phase. We investigated how this speedup and phase distortion depend on the individual segments of the skull. We found that the distortion was smallest for the parietal regions (Fig. 6), with a value 1.8 times smaller than for the frontal and 1.7 times smaller than the occipital regions (Table 1). A two-way ANOVA revealed a significant modulation of the phase distortion by the skull position ($F(360, 654) = 5.08$, $p = 1.5 \times 10^{-72}$) and by subject ($F(2, 654) = 694.63$, $p = 1.7 \times 10^{-162}$).

The speedup and the associated phase distortion should be linearly proportional to skull thickness (see Materials and Methods). This proportionality has been demonstrated previously [49]. Indeed, we confirmed these findings (Fig. 7). In the 3 skulls, skull thickness explained 73%, 78%, and 81% of the variance in the phase aberration, respectively. An ANCOVA model, again with a continuous factor of thickness and a discrete factor of subject, found a significant effect of thickness ($F(1, 464) = 1175.53$, $p = 2.9 \times 10^{-129}$) as well as an effect of subject ($F(2, 464) = 55.92$, $p = 1.7 \times 10^{-22}$) and thickness×subject interaction ($F(2, 464) = 142.78$, $p = 4.8 \times 10^{-49}$). Thus, the linear relationship between the phase aberration and skull thickness, albeit robust within an individual, is variable across individuals.

The previous finding suggests an appreciable difference in the average speed of sound across the skulls. We investigated the speed of sound across the skulls and across the individual segments of each skull (Fig. 8). There was a substantial variability in the speed of sound, both across and within the subjects. In particular, the three skulls showed a mean±SD of 2451±383 m/s, 2401±307 m/s, and 2887±412 m/s, respectively. Although there was a trend for the speed of sound to be lower for the parietal bone (Table 1) compared to frontal and occipital bone, this was not consistent across subjects (Fig. 8). A two-way ANOVA confirmed the significant variability of the speed of sound by skull position ($F(359, 652) = 1.29$, $p = 0.0024$) and by subject ($F(2, 652) = 173.07$, $p = 5.1 \times 10^{-61}$).

4. Discussion

In this study, we investigated the transmission and phase distortion of ultrasound across intact human skulls.

We found that 500 kHz ultrasound—a common frequency for transcranial applications in humans—was most effectively transmitted through segments of the parietal bone (Fig. 3), in all three *ex-vivo* specimens. We further found that the transmission was strongly dependent on the skull thickness: the thinner the skull, the more effective the transmission (Fig. 5). Since parietal bone was found to be the thinnest on average (Fig. 4, Table 1), this negative correlation can partially explain the facilitated transmission through the parietal bone.

A negative correlation between skull thickness and ultrasound transmission could be expected, but has not, to our knowledge, been shown explicitly. Our direct measurements of skull thickness using a caliper uncovered a surprisingly tight relationship (64% of variance explained, mean across 3 skulls) between the skull thickness and ultrasound transmission. However, the slopes of the dependence on the thickness varied across the 3 skulls. In addition—and as observed in previous studies [41, 43, 44]—we found a significant difference in the average transmission across the 3 skulls. These subject-specific factors complicate a parsimonious description of ultrasound transmission based on skull thickness alone.

We found that the speedup of ultrasound due to the propagation through the skull bone, and the associated phase distortion, are also smallest over parietal bone segments (Fig. 6). This finding can be explained by our (Fig. 7) and previous [49] findings that the speedup

and phase shift are proportional to skull thickness. The slope of this dependence, which is a function of the average speed of sound through the skull (see Materials and Methods), varied significantly across the skulls. This variability has been observed also in previous studies, but can be accounted for using CT skull density measurements [55, 64].

The data provided in this study corroborate the notion of substantial variability of acoustic properties across individuals [32, 41–44]. In addition to the inter-subject variability, we have shown, in a systematic experiment, that there is substantial skull location-dependent variability. Transmission and phase shift comprised a well-defined function of skull location (Fig. 3, Fig. 6). The speed of sound, in contrast, showed a much less predictable pattern (Fig. 8).

The primary goal of our study was to identify the regions of the skull that provide optimal transmission. Although our robotic system allowed us to assess the acoustic properties across the perimeter of the skull, it only enabled us to operate along the middle segments of the skull. Acoustic properties for more dorsal portion of calvariae are to be found elsewhere [42, 43]. In addition, degassed ex-vivo skulls show somewhat larger attenuation than freshly excised skulls [41]. The values presented in this study should be taken as relative—with respect to anatomical location or skull thickness, rather than absolute. While our subjects were limited to people of relatively old age, no significant correlation has been found between age and bone density, diploe thickness, or cranial vault thickness [65–67].

The thickness measurements revealed a surprisingly tight relationship between ultrasound transmission and skull thickness. The correlation between skull thickness and ultrasound transmission may be even higher if we did not assume a uniform thickness of the skull portion intersecting each measured beam, i.e., if the caliper measurements were performed across the entire skull. This relationship invites future investigations with the goal to account for the attenuation of ultrasound transmission through the skull based on CT [68], MRI [68, 69], or other imaging modalities [57].

The importance of selecting appropriate sonication path through the skull is highlighted in Fig. 9, which shows the distribution of intensity attenuation through parietal, frontal, and occipital segments across all three skulls. The figure demonstrates that sonicating the same target through different sections of the skull could deliver intensities that differ by an order of magnitude if this factor is not accounted for. Moreover, the figure reveals the amount of variability in the intensity attenuation across the individual skull segments. Applying ultrasound through occipital or frontal parts of the skull makes the dose delivered into a target essentially unpredictable. The variability is much smaller when ultrasound is delivered through the parietal bone, increasing the operator’s confidence in the delivered dose.

In summary, we measured the acoustic properties throughout the perimeter of intact human *ex-vivo* skulls. We found that regions of the parietal bone provide much more effective transmission and lower phase distortion than frontal and occipital regions. We further found that the ultrasound transmission strongly depends on the skull thickness. These data inform future approaches to compensate for ultrasound skull aberrations and guide the design of future devices for safe, effective, and reproducible transcranial ultrasound therapies.

Acknowledgements

This work was supported by the National Institutes of Health (grants R00NS100986 and F32MH123019).

Biographies

Thomas S. Riis (M’76--SM’81--F’87) and all authors may include biographies. Biographies are often not included in conference-related papers. This author became a Member (M) of IEEE in 1976, a Senior Member (SM) in 1981, and a Fellow (F) in 1987. The first paragraph may contain a place and/or date of birth (list place, then date). Next, the author’s educational background is listed. The degrees should be listed with type of degree in what field, which institution, city, state, and country, and year the degree was earned. The author’s major field of study should be lower-cased.

The second paragraph uses the pronoun of the person (he or she) and not the author’s last name. It lists military and work experience, including summer and fellowship jobs. Job titles are capitalized. The current job must have a location; previous positions may be listed without one. Information concerning previous publications may be included. Try not to list more than three books or published articles. The format for listing publishers of a book within the biography is: title of book (publisher name, year) similar to a reference. Current and previous research interests end the paragraph. The third paragraph begins with the author’s title and last name (e.g., Dr. Smith, Prof. Jones, Mr. Kajor, Ms. Hunter). List any memberships in professional societies other than the IEEE. Finally, list any awards and work for IEEE committees and publications. If a photograph is provided, it should be of good quality, and professional-looking. Following are two examples of an author’s biography.

Taylor D. Webb was born in Greenwich Village, New York, NY, USA in 1977. He received the B.S. and M.S. degrees in aerospace engineering from the University of Virginia, Charlottesville, in 2001 and the Ph.D. degree in mechanical engineering from Drexel University, Philadelphia, PA, in 2008.

From 2001 to 2004, he was a Research Assistant with the Princeton Plasma Physics Laboratory. Since 2009, he has been an Assistant Professor with the Mechanical Engineering Department, Texas A&M University, College Station. He is the author of three books, more than 150 articles, and more than 70 inventions. His research interests include high-pressure and high-density nonthermal plasma discharge processes and applications, microscale plasma discharges, discharges in liquids, spectroscopic diagnostics, plasma

propulsion, and innovation plasma applications. He is an Associate Editor of the journal *Earth, Moon, Planets*, and holds two patents.

Dr. Author was a recipient of the International Association of Geomagnetism and Aeronomy Young Scientist Award for Excellence in 2008, and the IEEE Electromagnetic Compatibility Society Best Symposium Paper Award in 2011.

\end{IEEEbiography}

Jan Kubanek, Jr. (M’87) received the B.S. degree in mechanical engineering from National Chung Cheng University, Chiayi, Taiwan, in 2004 and the M.S. degree in mechanical engineering from National Tsing Hua University, Hsinchu, Taiwan, in 2006. He is currently pursuing the Ph.D. degree in mechanical engineering at Texas A&M University, College Station, TX, USA.

From 2008 to 2009, he was a Research Assistant with the Institute of Physics, Academia Sinica, Tapei, Taiwan. His research interest includes the development of surface processing and biological/medical treatment techniques using nonthermal atmospheric pressure plasmas, fundamental study of plasma sources, and fabrication of micro- or nanostructured surfaces.

Mr. Author’s awards and honors include the Frew Fellowship (Australian Academy of Science), the I. I. Rabi Prize (APS), the European Frequency and Time Forum Award, the Carl Zeiss Research Award, the William F. Meggers Award and the Adolph Lomb Medal (OSA).

References

[1]. Hynynen K, Jolesz FA, Demonstration of potential noninvasive ultrasound brain therapy through an intact skull, Ultrasound in medicine & biology 24 (2) (1998) 275–283. [PubMed: 9550186]

[2]. Landhuis E, Ultrasound for the brain, Nature 551 (7679) (2017) 257–259.

[3]. Meng Y, Hynynen K, Lipsman N, Applications of focused ultrasound in the brain: From thermoablation to drug delivery, Nature Reviews Neurology (2020) 1–16. [PubMed: 31827266]

[4]. Ghanouni P, Pauly KB, Elias WJ, Henderson J, Sheehan J, Monteith S, Wintermark M, Transcranial MRI-guided focused ultrasound: a review of the technologic and neurologic applications, American Journal of Roentgenology 205 (1) (2015) 150–159. [PubMed: 26102394]

[5]. Giordano M, Caccavella VM, Zaed I, Manzillo LF, Montano N, Olivi A, Polli FM, Comparison between deep brain stimulation and magnetic resonance-guided focused ultrasound in the treatment of essential tremor: a systematic review and pooled analysis of functional outcomes, Journal of Neurology, Neurosurgery & Psychiatry 91 (12) (2020) 1270–1278.

[6]. Carpentier, Canney M, Vignot A, Reina V, Beccaria K, Horodyckid C, Karachi C, Leclercq D, Lafon C, Chapelon J-Y, et al. , Clinical trial of blood-brain barrier disruption by pulsed ultrasound, Science Transl. Medicine 8 (343) (2016) 343.

[7]. Lipsman N, Meng Y, Bethune AJ, Huang Y, Lam B, Masellis M, Herrmann N, Heyn C, Aubert I, Boutet A, et al. , Blood–brain barrier opening in Alzheimer's disease using MR-guided focused ultrasound, Nature Communications 9 (1) (2018) 2336.

[8]. Anastasiadis P, Winkles JA, Kim AJ, Woodworth GF, Focused ultrasound-mediated blood-brain barrier disruption for enhanced drug delivery to brain tumors, in: Nanotherapy for Brain Tumor Drug Delivery, Springer, 2021, pp. 205–223.

[9]. Chen KT, Wei KC, Liu HL, Theranostic strategy of focused ultrasound induced blood-brain barrier opening for CNS disease treatment (2019). doi:10.3389/fphar.2019.00086.

[10]. Airan RD, Meyer RA, Ellens NP, Rhodes KR, Farahani K, Pomper MG, Kadam SD, Green JJ, Noninvasive targeted transcranial neuromodulation via focused ultrasound gated drug release from nanoemulsions, Nano Letters 17 (2) (2017) 652–659. [PubMed: 28094959]

[11]. Wang JB, Aryal M, Zhong Q, Vyas DB, Airan RD, Noninvasive ultrasonic drug uncaging maps whole-brain functional networks, Neuron 100 (3) (2018) 728–738. [PubMed: 30408444]

[12]. Lea-Banks H, Meng Y, Wu S-K, Belhadjhamida R, Hamani C, Hynynen K, Ultrasound-sensitive nanodroplets achieve targeted neuromodulation, Journal of Controlled Release (2021).

[13]. Lea-Banks H, O'Reilly MA, Hynynen K, Ultrasound-responsive droplets for therapy: A review, Journal of Controlled Release 293 (November 2018) (2019) 144–154. doi:10.1016/j.jconrel.2018.11.028. [PubMed: 30503398]

[14]. Kubanek J, Neuromodulation with transcranial focused ultrasound, Neurosurgical Focus 44 (2) (2018) E14.

[15]. Tyler WJ, Lani SW, Hwang GM, Ultrasonic modulation of neural circuit activity, Current opinion in neurobiology 50 (2018) 222–231. [PubMed: 29674264]

[16]. Blackmore J, Shrivastava S, Sallet J, Butler CR, Cleveland RO, Ultrasound neuromodulation: A review of results, mechanisms and safety, Ultrasound in medicine & biology 45 (7) (2019) 1509–1536. [PubMed: 31109842]

[17]. Kubanek J, Brown J, Ye P, Pauly KB, Moore T, Newsome W, Remote, brain region–specific control of choice behavior with ultrasonic waves, Science Advances 6 (21) (2020) eaaz4193. [PubMed: 32671207]

[18]. Sanguinetti JL, Hameroff S, Smith EE, Sato T, Daft CM, Tyler WJ, Allen JJ, Transcranial focused ultrasound to the right prefrontal cortex improves mood and alters functional connectivity in humans, Frontiers in Human Neuroscience 14 (2020) 52. [PubMed: 32184714]

[19]. Badran BW, Caulfield KA, Stomberg-Firestein S, Summers PM, Dowdle LT, Savoca M, Li X, Austelle CW, Short EB, Borckardt JJ, et al. , Sonication of the anterior thalamus with mri-guided transcranial focused ultrasound (tfus) alters pain thresholds in healthy adults: A double-blind, sham-controlled study, Brain Stimulation 13 (6) (2020) 1805–1812. [PubMed: 33127579]

[20]. Verhagen L, Gallea C, Folloni D, Constans C, Jensen DE, Ahnine H, Roumazeilles L, Santin M, Ahmed B, Lehéricy S, et al. , Offline impact of transcranial focused ultrasound on cortical activation in primates, Elife 8 (2019) e40541. [PubMed: 30747105]

[21]. Fouragnan EF, Chau BK, Folloni D, Kolling N, Verhagen L, Klein-Flügge M, Tankelevitch L, Papageorgiou GK, Aubry J-F, Sallet J, et al. , The macaque anterior cingulate cortex translates counter-factual choice value into actual behavioral change, Nature neuroscience 22 (5) (2019) 797–808. [PubMed: 30988525]

[22]. Khalighinejad N, Bongioanni A, Verhagen L, Folloni D, Attali D, Aubry J-F, Sallet J, Rushworth MF, A basal forebrain-cingulate circuit in macaques decides it is time to act, Neuron 105 (2) (2020) 370–384. [PubMed: 31813653]

[23]. Velling V, Shklyaruk S, Modulation of the functional state of the brain with the aid of focused ultrasonic action, Neuroscience and behavioral physiology 18 (5) (1988) 369–375. [PubMed: 3063995]

[24]. Dallapiazza RF, Timbie KF, Holmberg S, Gatesman J, Lopes MB, Price RJ, Miller GW, Elias WJ, Noninvasive neuromodulation and thalamic mapping with low-intensity focused ultrasound, Journal of Neurosurgery (2017) 1–10.

[25]. Fomenko, Neudorfer C, Dallapiazza RF, Kalia SK, Lozano AM, Low-intensity ultrasound neuromodulation: An overview of mechanisms and emerging human applications, Brain stimulation (2018).

[26]. Chang WS, Jung HH, Zadicario E, Rachmilevitch I, Tlusty T, Vitek S, Chang JW, Factors associated with successful magnetic resonance-guided focused ultrasound treatment: efficiency of acoustic energy delivery through the skull, Journal of neurosurgery 124 (2) (2016) 411–416. [PubMed: 26361280]

[27]. Mueller JK, Ai L, Bansal P, Legon W, Numerical evaluation of the skull for human neuromodulation with transcranial focused ultrasound, Journal of neural engineering 14 (6) (2017) 066012. [PubMed: 28777075]

[28]. Chen H, Konofagou EE, The size of blood–brain barrier opening induced by focused ultrasound is dictated by the acoustic pressure, Journal of Cerebral Blood Flow & Metabolism 34 (7) (2014) 1197–1204. [PubMed: 24780905]

[29]. Lee W, Kim H-C, Jung Y, Chung YA, Song I-U, Lee J-H, Yoo SS, Transcranial focused ultrasound stimulation of human primary visual cortex, Scientific Reports 6 (2016).

[30]. Braun V, Blackmore J, Cleveland RO, Butler CR, Transcranial ultrasound stimulation in humans is associated with an auditory confound that can be effectively masked, Brain stimulation 13 (6) (2020) 1527–1534. [PubMed: 32891872]

[31]. Plaksin M, Kimmel E, Shoham S, Cell-type-selective effects of intramembrane cavitation as a unifying theoretical framework for ultrasonic neuromodulation, eneuro 3 (3) (2016).

[32]. Ammi Y, Mast TD, Huang I-H, Abruzzo TA, Coussios C-C, Shaw GJ, Holland CK, Characterization of ultrasound propagation through ex-vivo human temporal bone, Ultrasound in medicine & biology 34 (10) (2008) 1578–1589. [PubMed: 18456391]

[33]. Purkayastha S, Sorond F, Transcranial doppler ultrasound: technique and application, in: Seminars in neurology, Vol. 32, NIH Public Access, 2012, p. 411. [PubMed: 23361485]

[34]. Wang Z, Komatsu T, Mitsumura H, Nakata N, Ogawa T, Iguchi Y, Yokoyama M, An uncovered risk factor of sonothrombolysis: substantial fluctuation of ultrasound transmittance through the human skull, Ultrasonics 77 (2017) 168–175. [PubMed: 28242510]

[35]. Soulioti DE, Espíndola D, Dayton PA, Pinton GF, Super-resolution imaging through the human skull, IEEE transactions on ultrasonics, ferroelectrics, and frequency control 67 (1) (2019) 25–36.

[36]. Brinker ST, Preiswerk F, White PJ, Mariano TY, McDannold NJ, Bubrick EJ, Focused Ultrasound Platform for Investigating Therapeutic Neuromodulation Across the Human Hippocampus, Ultrasound in Medicine and Biology 46 (5) (2020) 1270–1274. doi:10.1016/j.ultrasmedbio.2020.01.007. [PubMed: 32088061]

[37]. Legon W, Sato TF, Opitz A, Mueller J, Barbour A, Williams A, Tyler WJ, Transcranial focused ultrasound modulates the activity of primary somatosensory cortex in humans, Nature Neuroscience 17 (2) (2014) 322–329. [PubMed: 24413698]

[38]. Lee W, Kim H, Jung Y, Song I-U, Chung YA, Yoo S-S, Image-guided transcranial focused ultrasound stimulates human primary somatosensory cortex, Scientific reports 5 (2015).

[39]. Legon W, Ai L, Bansal P, Mueller JK, Neuromodulation with single-element transcranial focused ultrasound in human thalamus, Human brain mapping 39 (5) (2018) 1995–2006. [PubMed: 29380485]

[40]. Legon W, Bansal P, Tyshynsky R, Ai L, Mueller JK, Transcranial focused ultrasound neuromodulation of the human primary motor cortex, Scientific reports 8 (1) (2018) 1–14. [PubMed: 29311619]

[41]. Fry FJ, Barger JE, Acoustical properties of the human skull, The Journal of the Acoustical Society of America 63 (5) (1978) 1576–1590. [PubMed: 690336]

[42]. White PJ, Clement GT, Hynynen K, Longitudinal and shear mode ultrasound propagation in human skull bone, Ultrasound in medicine & biology 32 (7) (2006) 1085–1096. [PubMed: 16829322]

[43]. Pichardo S, Sin VW, Hynynen K, Multi-frequency characterization of the speed of sound and attenuation coefficient for longitudinal transmission of freshly excised human skulls, Physics in Medicine & Biology 56 (1) (2010) 219. [PubMed: 21149950]

[44]. Pichardo S, Moreno-Hernández C, Drainville RA, Sin V, Curiel L, Hynynen K, A viscoelastic model for the prediction of transcranial ultrasound propagation: application for the estimation of shear acoustic properties in the human skull, Physics in Medicine & Biology 62 (17) (2017) 6938. [PubMed: 28783716]

[45]. Fry F, Transkull transmission of an intense focused ultrasonic beam, Ultrasound in medicine & biology 3 (2–3) (1977) 179–184. [PubMed: 595211]

[46]. Barger JE, Attenuation and dispersion of ultrasound in cancellous bone, Ultrasonic Tissue Characterization 11 (1979) 197–201.

[47]. Evans J, Tavakoli M, Ultrasonic attenuation and velocity in bone, Physics in Medicine & Biology 35 (10) (1990) 1387. [PubMed: 2243843]

[48]. Tavakoli M, Evans J, Dependence of the velocity and attenuation of ultrasound in bone on the mineral content, Physics in Medicine & Biology 36 (11) (1991) 1529. [PubMed: 1754623]

[49]. Clement G, Hynynen K, Correlation of ultrasound phase with physical skull properties, Ultrasound in medicine & biology 28 (5) (2002) 617–624. [PubMed: 12079698]

[50]. Pinton G, Aubry J-F, Bossy E, Muller M, Pernot M, Tanter M, Attenuation, scattering, and absorption of ultrasound in the skull bone, Medical physics 39 (1) (2012) 299–307. [PubMed: 22225300]

[51]. Hynynen K, Sun J, Trans-skull ultrasound therapy: the feasibility of using image-derived skull thickness information to correct the phase distortion, IEEE transactions on ultrasonics, ferroelectrics, and frequency control 46 (3) (1999) 752–755.

[52]. Aarnio J, Clement GT, Hynynen K, A new ultrasound method for determining the acoustic phase shifts caused by the skull bone, Ultrasound in medicine & biology 31 (6) (2005) 771–780. [PubMed: 15936493]

[53]. White P, Clement G, Hynynen K, Local frequency dependence in transcranial ultrasound transmission, Physics in Medicine & Biology 51 (9) (2006) 2293. [PubMed: 16625043]

[54]. Marsac L, Chauvet D, La Greca R, Boch A-L, Chaumoitre K, Tanter M, Aubry J-F, Ex vivo optimisation of a heterogeneous speed of sound model of the human skull for non-invasive transcranial focused ultrasound at 1 mhz, International Journal of Hyperthermia 33 (6) (2017) 635–645. [PubMed: 28540778]

[55]. Webb TD, Leung SA, Rosenberg J, Ghanouni P, Dahl JJ, Pelc NJ, Pauly KB, Measurements of the relationship between ct hounsfield units and acoustic velocity and how it changes with photon energy and reconstruction method, IEEE transactions on ultrasonics, ferroelectrics, and frequency control 65 (7) (2018) 1111–1124.

[56]. Leung SA, Webb TD, Bitton RR, Ghanouni P, Pauly KB, A rapid beam simulation framework for transcranial focused ultrasound, Scientific reports 9 (1) (2019) 1–11. [PubMed: 30626917]

[57]. Deng L, Hughes A, Hynynen K, A noninvasive ultrasound resonance method for detecting skull induced phase shifts may provide a signal for adaptive focusing, IEEE Transactions on Biomedical Engineering 67 (9) (2020) 2628–2637. [PubMed: 31976875]

[58]. Ammi Y, Mast TD, Huang I-H, Abruzzo TA, Coussios C-C, Shaw GJ, Holland CK, Characterization of ultrasound propagation through ex-vivo human temporal bone., Ultrasound in medicine & biology 34 (10) (2008) 1578–1589. doi:10.1016/j.ultrasmedbio.2008.02.012. [PubMed: 18456391]

[59]. Phipps MA, Jonathan SV, Yang PF, Chaplin V, Chen LM, Grissom WA, Caskey CF, Considerations for ultrasound exposure during transcranial MR acoustic radiation force imaging, Scientific Reports 9 (1) (2019) 1–11. doi:10.1038/s41598-019-52443-8. URL 10.1038/s41598-019-52443-8 [PubMed: 30626917]

[60]. Eames MD, Hananel A, Snell JW, Kassell NF, Aubry JF, Transcranial focused ultrasound without hair shaving: Feasibility study in an ex vivo cadaver model, Journal of Therapeutic Ultrasound 1 (1) (2014) 2–7. doi:10.1186/2050-5736-1-24.

[61]. Alexander SL, Rafaels K, Gunnarsson CA, Weerasooriya T, Structural analysis of the frontal and parietal bones of the human skull, Journal of the Mechanical Behavior of Biomedical Materials 90 (November 2018) (2019) 689–701. doi:10.1016/j.jmbbm.2018.10.035. URL 10.1016/j.jmbbm.2018.10.035 [PubMed: 30530225]

[62]. Crocco M, Pellegretti P, Sciallero C, Trucco A, Combining multipulse excitation and chirp coding in contrast-enhanced ultrasound imaging, Measurement Science and Technology 20 (10) (2009) 104017.

[63]. Callegari S, Ricci M, Caporale S, Monticelli M, Eroli M, Senni L, Rovatti R, Setti G, Burrascano P, From chirps to random-fm excitations in pulse compression ultrasound systems, in: 2012 IEEE International Ultrasonics Symposium, IEEE, 2012, pp. 471–474.

[64]. Aubry J-F, Tanter M, Pernot M, Thomas J-L, Fink M, Experimental demonstration of noninvasive transskull adaptive focusing based on prior computed tomography scans, The Journal of the Acoustical Society of America 113 (1) (2003) 84–93. doi:10.1121/1.1529663. [PubMed: 12558249]

[65]. Lynnerup N, Cranial thickness in relation to age, sex and general body build in a Danish forensic sample, Forensic Science International 117 (1–2) (2001) 45–51. doi:10.1016/S0379-0738(00)00447-3. [PubMed: 11230945]

[66]. Lynnerup N, Astrup JG, Sejrsen B, Thickness of the human cranial diploe in relation to age, sex and general body build., Head & face medicine 1 (2005) 13. doi:10.1186/1746-160x-1-13. [PubMed: 16364185]

[67]. De Boer HH, Van der Merwe AE, Soerdjbalie-Maikoe VV, Human cranial vault thickness in a contemporary sample of 1097 autopsy cases: relation to body weight, stature, age, sex and ancestry, International Journal of Legal Medicine 130 (5) (2016) 1371–1377. doi:10.1007/s00414-016-1324-5. [PubMed: 26914798]

[68]. Acoustic Attenuation: Multifrequency Measurement and Relationship to CT and MR Imaging., IEEE transactions on ultrasonics, ferroelectrics, and frequency control 68 (5) (2021) 1532–1545. doi:10.1109/TUFFC.2020.3039743.

[69]. Miller GW, Eames M, Snell J, Aubry J-F, Ultrashort echo-time mri versus ct for skull aberration correction in mr-guided transcranial focused ultrasound: In vitro comparison on human calvaria, Medical physics 42 (5) (2015) 2223–2233. [PubMed: 25979016]

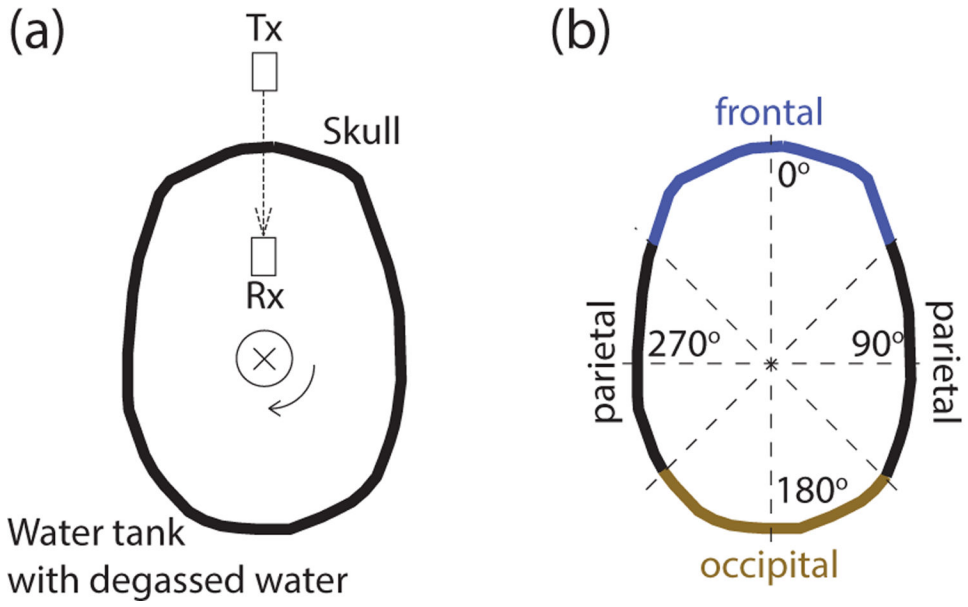

Figure 1: Through-transmit measurements across intact skulls.

(a) Top view of the setup. Degassed and hydrated *ex-vivo* skulls were held by a robotic arm and were secured to the skull using two opposing magnets positioned at the center of the sagittal suture (the thin circle shows the position of the magnets). This robotic arm, connected to the magnet at the top of the skull, allowed us to electronically rotate the skull and so collect through-transmit measurements over individual segments of the skull within the imaging plane. The through-transmit measurements were achieved using a transmitting (Tx) and a receiving (Rx) transducer facing each other at a distance of 100 mm. The direction of ultrasound transmission is indicated by the dashed arrow. The through-transmit measurements were acquired at each rotation step of 1 degree. (b) Parameterization of the skull bone into parietal (45–135 and 225–315 degrees), occipital (135–225 degrees), and frontal (315–45 degrees) regions.

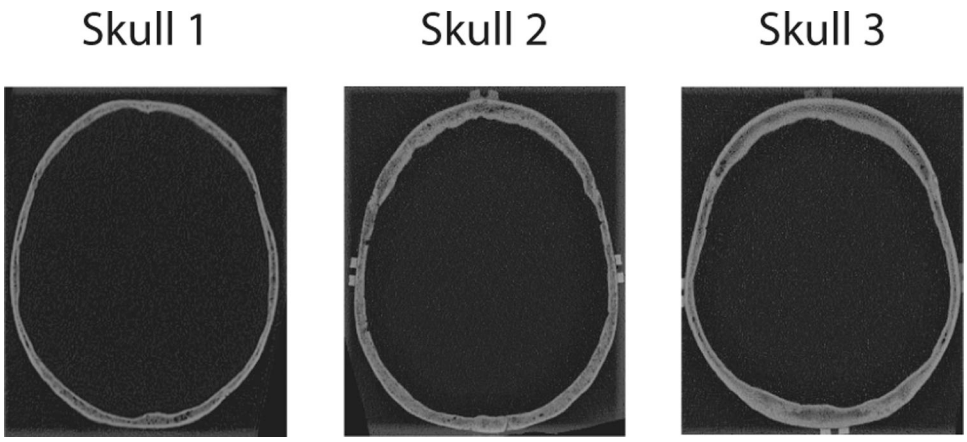

Figure 2: Subjects.

CT scans for the three *ex-vivo* skulls used in this study. The images were taken at the through-transmit plane.

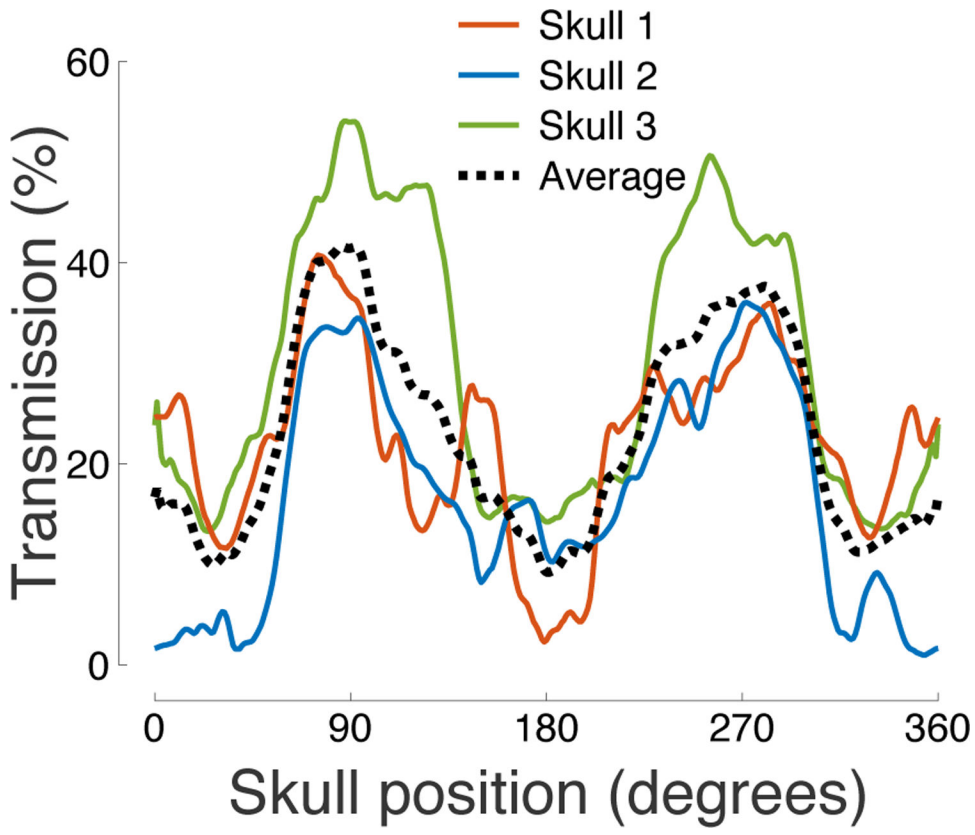

Figure 3: Ultrasound transmission throughout the skull.

The figure shows the relative pressure attenuation (skull versus no skull) for each measured segment of the skull. The carrier frequency was 500 kHz.

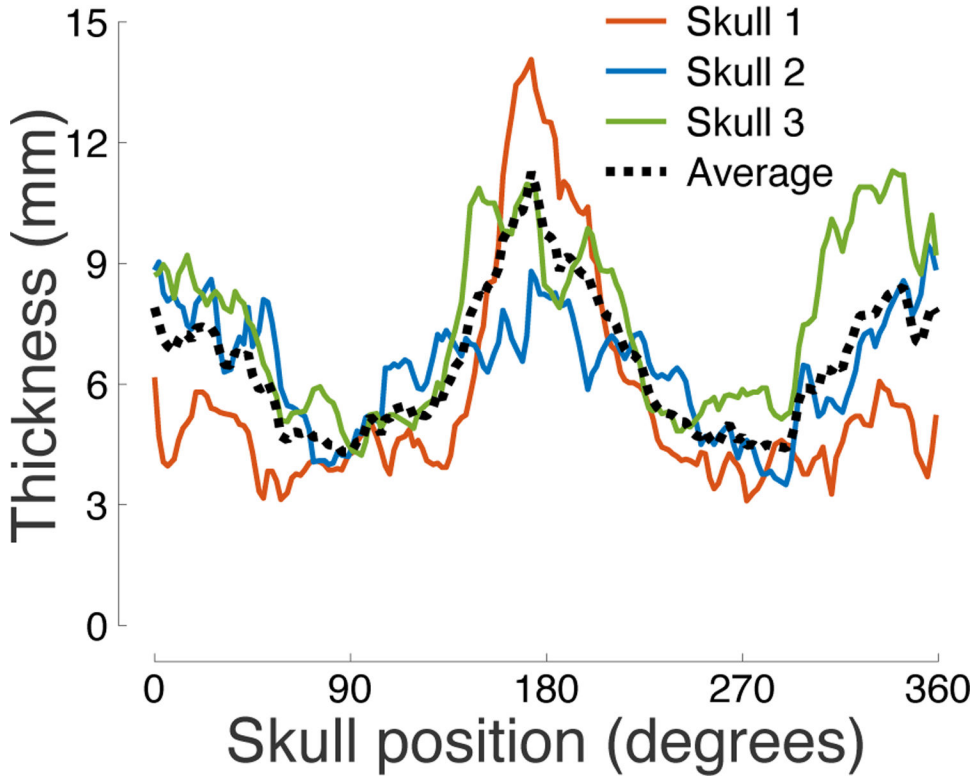

Figure 4: Skull thickness across angular position.

Mean thickness of each segment of the skull within the through-transmit plane. Three independent measurements were taken at each position.

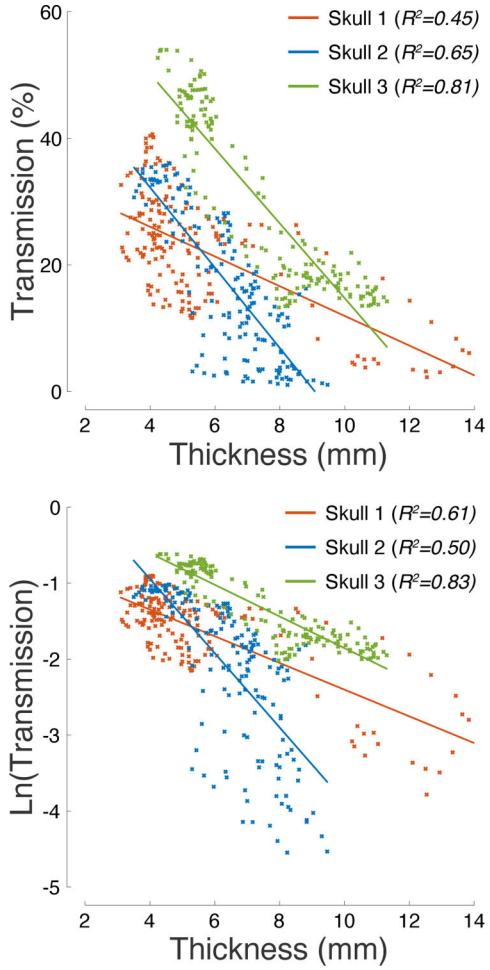

Figure 5: Ultrasound transmission is strongly governed by skull thickness.

Ultrasound pressure transmission (top) and its natural logarithm (bottom) as a function of skull thickness. The R^2 values listed in the inset provide the amount of variance explained by the linear fits superimposed on the plots.

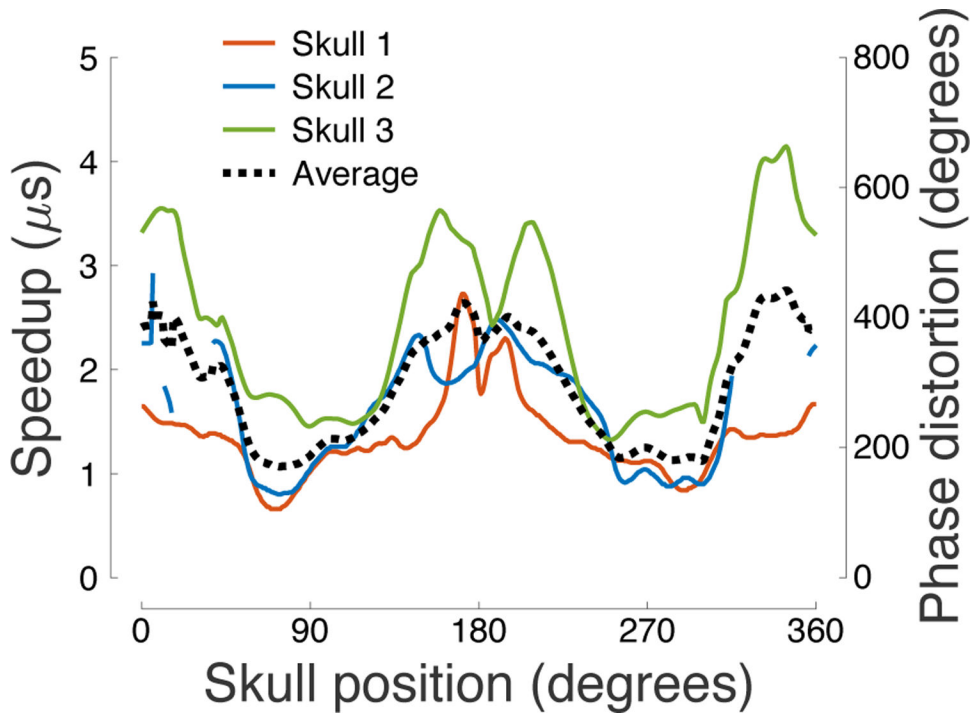

Figure 6: Speedup and phase distortion across the skull.

Ultrasound speedup through the skull (τ) and the associated phase distortion ($\omega\tau$) as a function of the skull position. Several segments of the occipital and frontal bones in Skull 2 provided extreme aberration, rendering the through-transmit cross-correlation unreliable; values for these segments are therefore not shown.

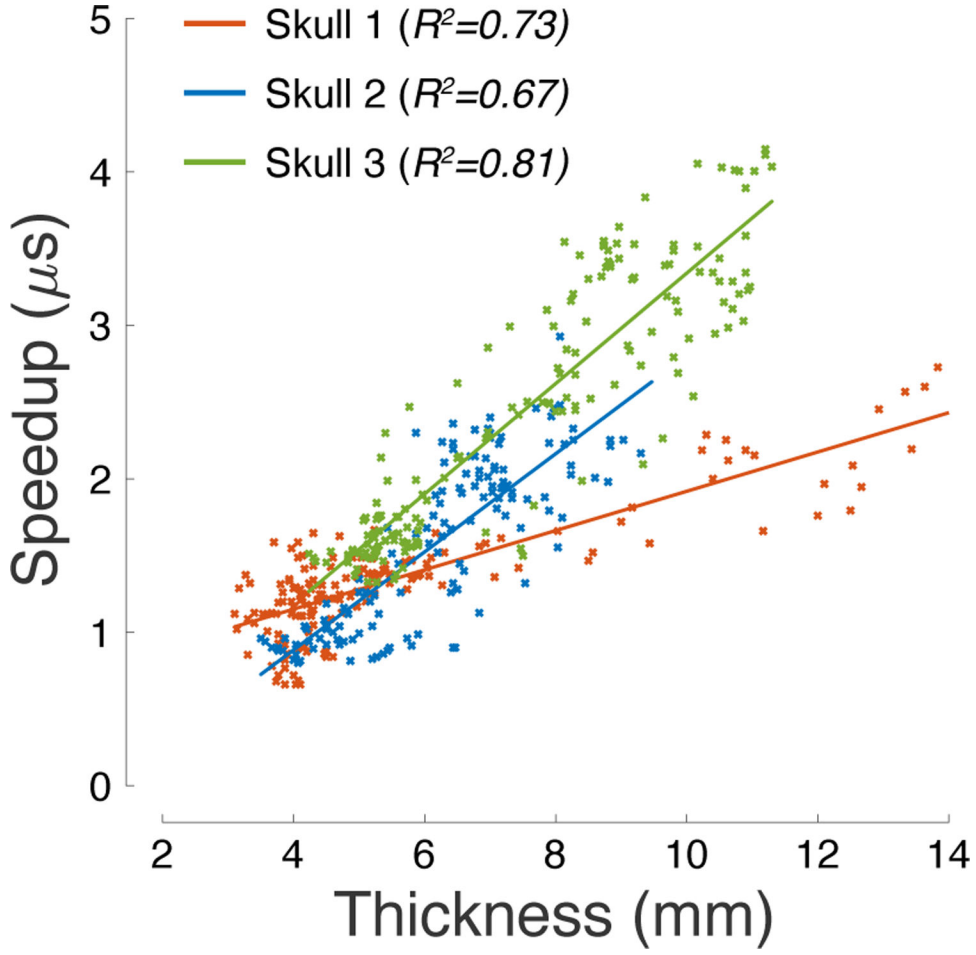

Figure 7: Ultrasound phase distortion is proportional to skull thickness.

Ultrasound speedup through individual segments of the skull as a function of skull thickness. The R^2 values listed in the inset provide the amount of variance explained by the linear fits superimposed on the plots.

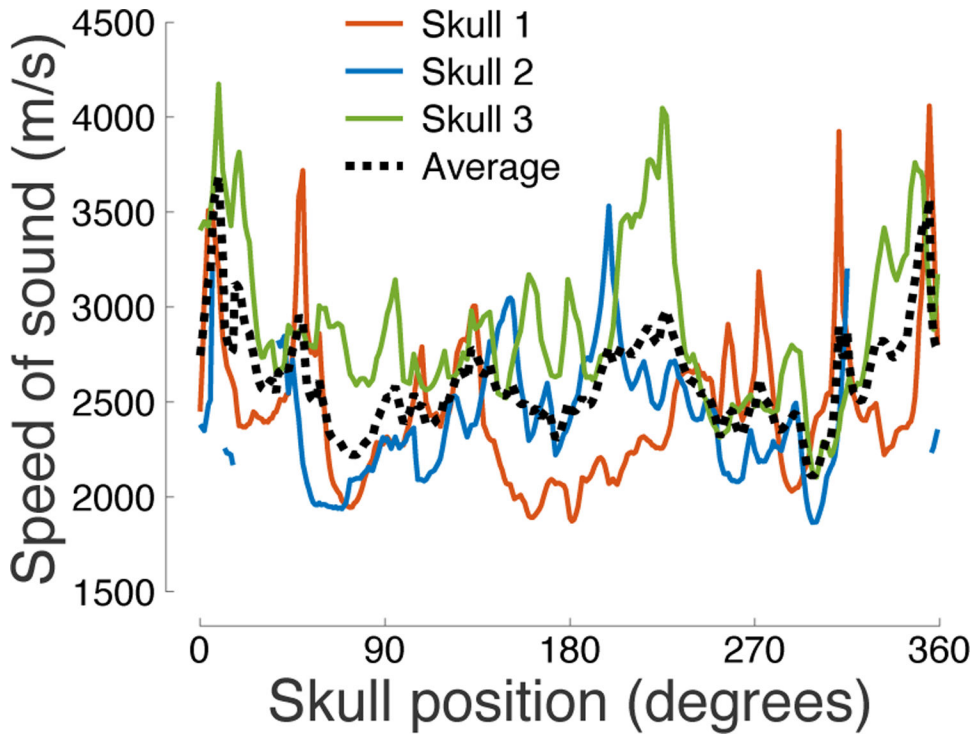

Figure 8: Speed of sound across the skull.

The speed of sound (c_s) determined from the through-transmit τ values (see Materials and Methods) as a function of the skull position.

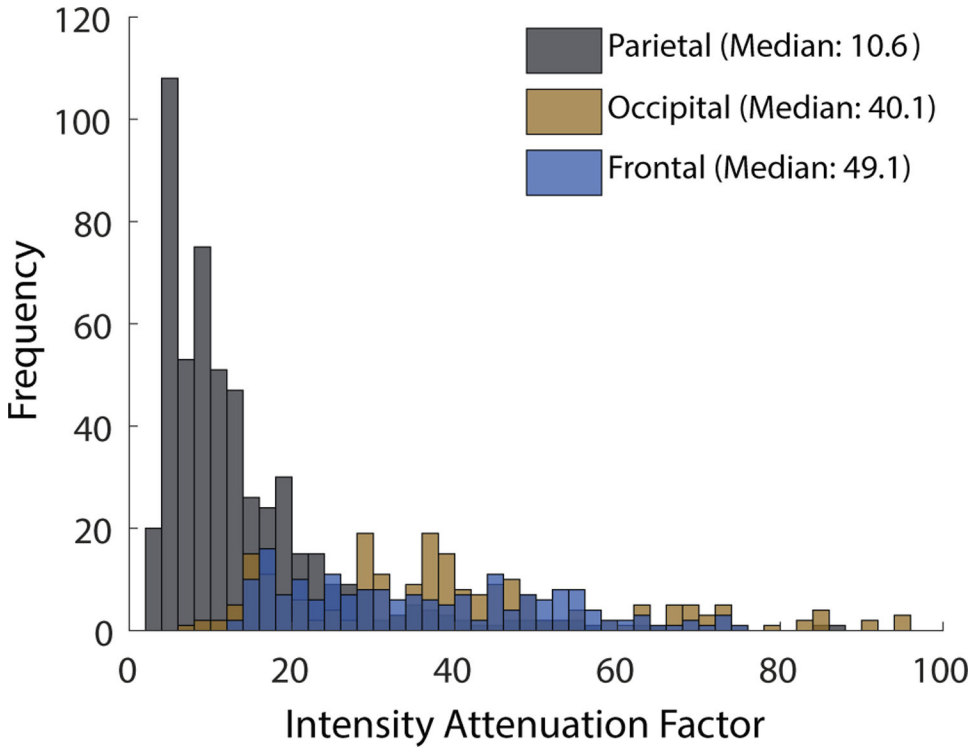

Figure 9: Intensity attenuation factor distribution by skull section.

Intensity attenuation factor (T^{-2}) varies significantly by region of the skull. The parietal bone's 5^{th} to 95^{th} percentile range is an order of magnitude lower than both the frontal and occipital regions.

Table 1:
Acoustic properties quantified over distinct skull regions.

The table lists the mean±SD transmission (T), speedup (τ), thickness (h), and speed of sound (cs) as a function of skull position (rows). The parietal optimum entry lists maximal transmission, minimal speedup, and minimal thickness, averaged across the 3 skulls.

	T (%)		τ (μS)		h (mm)		c_s (m/s)	
	Mean	***SD***	**Mean**	***SD***	**Mean**	***SD***	**Mean**	***SD***
Frontal	13.2	1.9	2.4	0.3	7.3	0.6	2871	289
Parietal	31.2	7.3	1.3	0.2	5.1	0.6	2486	193
Par. optimum	41.6	9.4	1.1	0.4	4.3	0.6		
Occipital	15.8	4.4	2.3	0.2	8.5	1.4	2603	160
All	22.9	10.2	1.8	0.6	6.5	1.7	2609	266